Interlayer interactions in $La_3Ni_2O_7$ under pressure: From $s^{\pm}$ to d_{xy}-wave superconductivity

Lauro B. Braz [1], George B. Martins [2], and Luis G. G. V. Dias da Silva [1]
[1]Instituto de Física, Universidade de São Paulo, Rua do Matão 1371, São Paulo, São Paulo 05508-090, Brazil
[2]Instituto de Física, Universidade Federal de Uberlândia, Uberlândia, Minas Gerais 38400-902, Brazil

(Received 10 March 2025; accepted 1 June 2025; published 7 July 2025)

We investigate the role of *interlayer* interaction terms in the competition between different superconducting gap symmetries in the bilayer nickelate $La_3Ni_2O_7$ under high pressure. We study a two-layer, two-orbital electron model that encompasses both intra- and interlayer Coulomb interaction terms within the matrix random-phase approximation. We find that interlayer interactions favor a d_{xy}-wave superconducting pairing symmetry over the $s^{\pm}$-wave symmetry, which has been found to prevail when interlayer interactions are disregarded. Moreover, our findings indicate that interlayer interactions enhance the interorbital pairing, incorporating contributions from all three electron pockets, arising from both $d_{3z^2-r^2}$ and $d_{x^2-y^2}$ orbital characters, resulting in nodes within the gap function (not present in the $s^{\pm}$-wave state) and consequently favoring the d_{xy}-wave pairing.

DOI: 10.1103/f4wf-56fl

I. INTRODUCTION

The recent discovery of high-temperature superconductivity in the Ruddlesden-Popper bilayer nickelate compound $La_3Ni_2O_7$ (LNO327) under high pressure [1–3] has sparked intense research on this new family of high-T_c materials [4]. Despite the rapid progress in the last two years, including recent reports of superconductivity on thin films at ambient pressure [5], several fundamental questions remain on the nature of the underlying pairing mechanism for superconductivity in these compounds.

For example, there has been an intense debate as to which low-energy *minimal* model to use when describing the superconducting phase. Density functional theory calculations [6–9] reveal that multiple bands, mainly formed by Ni-centered in-plane $d_{x^2-y^2}$ and out-of-plane $d_{3z^2-r^2}$ orbitals, along with oxygen-centered p orbitals cross the Fermi level, forming two electron pockets (α, β) with mixed orbital character and one hole pocket (γ) primarily associated with the Ni $d_{3z^2-r^2}$ orbital [6]. These bands can be described by a two-layer, two-orbital minimal tight-binding model [6,7,9], which has been investigated with interlayer interactions within a localized electron picture [10] and without interlayer interactions in an itinerant electron picture [8,9,11–13].

Using these models, some RPA calculations suggest that $s^{\pm}$-wave pairing is the dominant superconducting instability [8,11,12,14–16], which can be driven by intra-orbital (π, 0) scattering between the β and the γ pockets [8], although the d-wave pairing channel is found to be close in energy to the s-wave pairing one [8,12].

By contrast, several works have brought up the possibility that d-wave symmetry is dominant in some regimes. These range from d-p hybridized single-orbital models showing cuprate-like $d_{x^2-y^2}$ symmetry [17] to two-orbital models based on Ni-e_g DFT bands [9], as well as the differences in the spin response in these cases [18]. Moreover, a recent paper [19] reports DFT + RPA calculations showing that the leading superconducting instability has d_{xy} symmetry, although a slight increase in the strength of the Ni-e_g crystal field splitting can change the pairing symmetry to $s^{\pm}$.

On the experimental side, recent explorations of the ambient pressure properties of LNO327 give indications that *interlayer* interactions can be relevant for the superconducting phase at high pressures. Neutron scattering experiments in polycrystalline samples show evidence of spin excitations in the inelastic channel, which are consistent with strong interlayer exchange couplings [20] while x-ray absorption measurements [21] revealed dispersive magnons and spin-density wave order patterns which are also consistent with interlayer magnetic exchange being about an order of magnitude larger than intralayer ones. In addition, recent RIXS experiments in LNO327 thin film samples show evidence of a strain-enhanced interlayer exchange interaction coupling [22].

In this work, we investigate the role of the interlayer Coulomb interaction terms in the competition between different superconducting gap symmetries in LNO327 under high pressure. We consider a two-layer, two-orbital electron model that includes both intra- and interlayer Coulomb interaction terms. Within the weak-to-intermediate-coupling matrix random-phase approximation (mRPA) [23–27], we find that interlayer interactions favor a d_{xy}-wave superconductivity over the $s^{\pm}$ state, which is known to dominate when such interlayer interactions are neglected [8,11,14]. Our mRPA calculations reveal that interlayer interactions enhance interorbital pairing involving contributions from *all three* pockets, creating nodes in the gap function (absent in the $s^{\pm}$-wave state) and thus favoring the d_{xy}-wave pairing.

We note that some very recent theoretical works [28,29] also report transitions from s-wave to d-wave pairing symmetry for larger interlayer interaction strengths in LNO327.

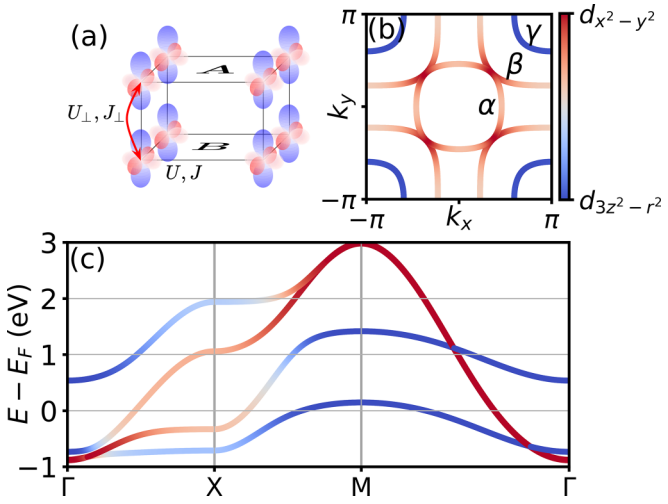

FIG. 1. Schematic representation of the bilayer $La_3Ni_2O_7$ model (a) with onsite U, J and interlayer $U_\perp, J_\perp$ Coulomb interaction and Hund's exchange coupling strengths. FS (b) and band structure (c) for the two-orbital $d_{3z^2-r^2}$ (blue color) and $d_{x^2-y^2}$ (red color) low-energy model.

Although these works use different methods (namely FLEX [28] and fRG [29]), the main results are qualitatively similar to the findings reported here.

This paper is organized as follows: In Sec. II, we present the interacting model for bilyer LNO327, including the band structure and both the onsite and interlayer interaction terms. We review the matrix-RPA methodology and describe the pairing gap calculation in Sec. III. Our results detailing the $s^{\pm}$-wave to d_{xy}-wave symmetry transition as the interlayer interaction increases are presented in Sec. IV, along with a discussion on the role of the charge susceptibility and the orbital contributions. Finally, our concluding remarks are presented in Sec. V.

II. MODEL

A. Band structure

In order to describe the (noninteracting) band structure of the system, we consider the four-band low-energy model of Refs. [6,12]. This tight-binding model involves two orbitals ($d_{x^2-y^2}$ and $d_{3z^2-r^2}$) per Ni atom in a unit cell with two Ni atoms (one for each layer) [as depicted in Fig. 1(a)] and hoppings up to second nearest neighbors. The non-interacting Hamiltonian reads

$$H_0 = \sum_{\boldsymbol{k}\sigma p\ell} \left(T^p_{\boldsymbol{k}} - \mu\right) c^\dagger_{\boldsymbol{k}p\ell\sigma} c_{\boldsymbol{k}p\ell\sigma} + \sum_{\boldsymbol{k}\sigma p} t^p_\perp (c^\dagger_{\boldsymbol{k}pA\sigma} c_{\boldsymbol{k}pB\sigma} + \text{H.c.}) + \sum_{\boldsymbol{k}\sigma (p\neq s)\ell} V_{\boldsymbol{k}} c^\dagger_{\boldsymbol{k}p\ell\sigma} c_{\boldsymbol{k}s\ell\sigma} + \sum_{\boldsymbol{k}\sigma (p\neq s)} V'_{\boldsymbol{k}} (c^\dagger_{\boldsymbol{k}pA\sigma} c_{\boldsymbol{k}sB\sigma} + \text{H.c.}), \tag{1}$$

where $c^\dagger_{\boldsymbol{k}p\ell\sigma}$ creates an electron with spin σ, in the orbital $p = \{x, z\}$ corresponding to $\{d_{x^2-y^2}, d_{3z^2-r^2}\}$, sublattice $\ell = \{A, B\}$, and momentum $\boldsymbol{k}$, μ is the chemical potential, and h.c. shortcuts Hermitian conjugate. In the following, we use the model parameters of Ref. [6], which include on-site energies (ϵ^p) and up to second-neighbor hoppings, such that

$$\begin{aligned} T^p_{\boldsymbol{k}} &= 2t^p_1(\cos k_x + \cos k_y) + 4t^p_2 \cos k_x \cos k_y + \epsilon^p, \\ V_{\boldsymbol{k}} &= 2t^{xz}_3(\cos k_x - \cos k_y), \\ V'_{\boldsymbol{k}} &= 2t^{xz}_4(\cos k_x - \cos k_y). \end{aligned} \tag{2}$$

For a valence of 2.5 electrons per Ni atom [30], the resulting Fermi surface (FS) and band structure are shown in Figs. 1(b) and 1(c), respectively, together with the respective Ni orbital contributions. The FS shows electron pockets α and β with a strong contribution from the $d_{x^2-y^2}$ orbital (red), consistent with ARPES results at ambient pressure [31,32]. The γ hole pocket at (π, π), however, is dominated by the $d_{3z^2-r^2}$ orbital (blue) and its presence has been linked to the onset of superconductivity in LNO327 and similar materials [8,33,34]. We notice that some of the bands show mixed orbital regions (nearly white) along the $\boldsymbol{\Gamma} - \boldsymbol{X}$ and $\boldsymbol{X} - \boldsymbol{M}$ high-symmetry paths [Fig. 1(c)].

B. Onsite and interlayer interactions

Our model Hamiltonian $H = H_0 + H_I$ involves both the noninteracting part described by H_0 as well as an interacting term (H_I) which includes both onsite (U, J) and interlayer ($U_\perp, J_\perp$) Coulomb and Hund's coupling interaction terms, as represented in Fig. 1(a). We remark that $J, J_\perp$ are the Hund's couplings and differ from the effective exchange interaction $\tilde{J}, \tilde{J}_\perp$ of strong-coupling models [14,15].

The interacting Hamiltonian for the two-orbital itinerant electron model is given by the onsite plus interlayer parts, $H_I = H_{\text{onsite}} + H_{\text{inter}}$, where the onsite term is given by

$$\begin{aligned} H_{\text{onsite}} = U \sum_{ij,p\ell} n_{ip\ell\uparrow} n_{ip\ell\downarrow} + (U' - J/2) \sum_{i\ell,p<q} n_{ip\ell} n_{iq\ell} \\ - 2J \sum_{i\ell,p<q} \boldsymbol{S}_{ip\ell} \cdot \boldsymbol{S}_{iq\ell} \\ + J' \sum_{i\ell,p<q} (c^\dagger_{ip\ell\uparrow} c^\dagger_{ip\ell\downarrow} c_{iq\ell\downarrow} c_{iq\ell\uparrow} + \text{H.c.}) \end{aligned} \tag{3}$$

and the interlayer term reads

$$\begin{aligned} H_{\text{inter}} = U_\perp \sum_{ij,p\sigma\bar{\sigma}} n_{ipA\sigma} n_{ipB\bar{\sigma}} + (U'_\perp - J_\perp/2) \sum_{i,p<q} n_{ipA} n_{iqB} \\ - 2J_\perp \sum_{i,p<q} \boldsymbol{S}_{ipA} \cdot \boldsymbol{S}_{iqB} \\ + J'_\perp \sum_{i,p<q} (c^\dagger_{ipA\uparrow} c^\dagger_{ipB\downarrow} c_{iqB\downarrow} c_{iqA\uparrow} + \text{H.c.}). \end{aligned} \tag{4}$$

In the above, $c^\dagger_{ip\ell\sigma}$ creates an electron with spin σ, in orbital p, layer $\ell = A, B$, at the (square) lattice site i. In addition, we use a shortcut notation for the density operator, $n_{ip\ell} = \sum_\sigma n_{ip\ell\sigma}$. In the present model, $U(U_\perp), U'(U'_\perp), J(J_\perp)$, and $J'(J'_\perp)$ are the onsite (intersite) Hubbard, interorbital Hubbard, Hund's exchange coupling, and pair-hopping interaction strengths, respectively. In the following, we assume local spin rotational invariance such that $J' = J(J'_\perp = J_\perp)$ [23,24].

The interacting part of the Hamiltonian, H_I, can conveniently be rewritten in momentum space as

$$H_I = \sum_{\boldsymbol{q}} \sum_{pqst\ell\ell'} (U_c)^{p\ell q\ell}_{s\ell' t\ell'} n_{p\ell q\ell}(-\boldsymbol{q}) n_{s\ell' t\ell'}(\boldsymbol{q}) + \sum_{\boldsymbol{q}} \sum_{pqst\ell\ell'} (U_s)^{p\ell q\ell}_{s\ell' t\ell'} \boldsymbol{S}_{p\ell q\ell}(-\boldsymbol{q}) \cdot \boldsymbol{S}_{s\ell' t\ell'}(\boldsymbol{q}), \quad (5)$$

where $n_{pAqA}(\boldsymbol{q}) = \sum_{\boldsymbol{k}\sigma} c^\dagger_{(\boldsymbol{k}+\boldsymbol{q})pA\sigma} c_{\boldsymbol{k}qA\sigma}$ is the charge density and $\boldsymbol{S}_{pAqA}(\boldsymbol{q}) = \sum_{\boldsymbol{k}\sigma\bar{\sigma}} c^\dagger_{(\boldsymbol{k}+\boldsymbol{q})pA\sigma} \boldsymbol{\sigma}_{\sigma\bar{\sigma}} c_{\boldsymbol{k}qA\bar{\sigma}}$ the spin density for layer A (similarly for layer B), with $\boldsymbol{\sigma}_{\sigma\bar{\sigma}}$ being the Pauli vector. The matrix elements of the charge and spin interaction matrices which connect Eq. (5) with Eqs. (3) and (4) are given by

$$\begin{aligned}
&(U_s)^{pApA}_{pApA} = U, \quad (U_s)^{pApA}_{qAqA} = U', \\
&(U_s)^{pAqA}_{pAqA} = (U_s)^{pAqA}_{qApA} = J, \\
&(U_c)^{pApA}_{pApA} = U, \quad (U_c)^{pApA}_{qAqA} = -U' + 2J, \\
&(U_c)^{pAqA}_{qApA} = J, \quad (U_c)^{pAqA}_{pAqA} = -J + 2U', \\
&(U_c)^{pApA}_{pBpB} = 2U_\perp, \quad (U_c)^{pApA}_{qBqB} = 2U'_\perp, \\
&(U_c)^{pAqA}_{pBqB} = (U_c)^{pAqA}_{qBpB} = 2J_\perp,
\end{aligned} \quad (6)$$

where A, B denote the respective layer index [35]. For simplicity, we assume spin rotational invariance such that the standard relationships $U' = U - 2J$ and $U'_\perp = U_\perp - 2J_\perp$ hold and we set $J = U/4$ and $J_\perp = U_\perp/4$, which is consistent with previous studies [7], although we have verified that this choice does not qualitatively alter our main results (see Appendix A). Notice that the interlayer interaction terms $(U_\perp, U'_\perp)$ appear only in the *charge* interaction matrices.

III. MATRIX RPA METHOD

A. Spin and charge susceptibilities

For completeness, we begin this section by briefly reviewing the RPA-enhanced spin and charge susceptibilities for the multiorbital model of Eq. (1). Following Ref. [23], the bare spin susceptibility is calculated from the spin-spin correlation function as

$$[\hat{\chi}]^{p\ell q\ell'}_{s\xi t\xi'}(\boldsymbol{q}, i\nu_m) = \int_0^{1/T} d\tau e^{i\nu_m \tau} \times \langle T_\tau \boldsymbol{S}_{p\ell q\ell'}(-\boldsymbol{q}, \tau) \cdot \boldsymbol{S}_{s\xi t\xi'}(\boldsymbol{q}, 0)\rangle, \quad (7)$$

where $i\nu_m$ denotes Matsubara bosonic frequencies, τ is the imaginary time, T is the temperature, and T_τ is the time-ordering operator. For the noninteracting model, the spin and charge susceptibilities are equivalent [23] and can be written in terms of the noninteracting Green's functions as

$$[\hat{\chi}]^{p\ell q\ell'}_{s\xi t\xi'}(\boldsymbol{q}, i\nu_m) = -\frac{T}{N} \sum_{\boldsymbol{k} i\omega_n} G_{s\xi p\ell}(\boldsymbol{k}, i\omega_n) \times G_{q\ell' t\xi'}(\boldsymbol{k} + \boldsymbol{q}, i\omega_n + i\nu_m), \quad (8)$$

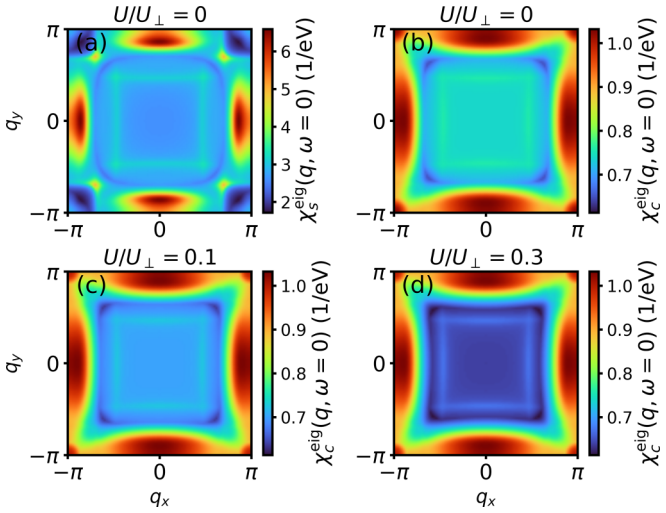

FIG. 2. Contour plots for the main eigenvalue of the spin (a) and charge (b)–(d) RPA susceptibility matrices for $U = 1.16$ eV and different $U_\perp/U$ ratios.

where

$$G_{s\xi p\ell}(\boldsymbol{k}, i\omega_n) = \sum_{\nu_k} \frac{\psi^{s\xi}_{\nu_k}(\boldsymbol{k}) \psi^{p\ell *}_{\nu_k}(\boldsymbol{k})}{i\omega_n - E_{\nu_k}(\boldsymbol{k})}, \quad (9)$$

and $\psi^{p\ell}_{\nu_k}(\boldsymbol{k})$ is a single-particle eigenfunction of H_0 [given by Eq. (1)] related to the $\nu_{\boldsymbol{k}}$-th electronic band with energy $E_{\nu_k}(\boldsymbol{k})$, and written in a basis where p and ℓ are good quantum numbers. The Matsubara summation is calculated numerically by using Ozaki's method [36]. In this work, we adopt $T = 0.02$ eV.

Within the mRPA, adding the onsite and interlayer interactions reduces to performing a matrix operation such that the spin and charge susceptibilities become

$$\hat{\chi}_s(\boldsymbol{q}, i\nu_m) = \hat{\chi}(\boldsymbol{q}, i\nu_m)[\hat{1} - \hat{U}_s \hat{\chi}(\boldsymbol{q}, i\nu_m)]^{-1}, \quad (10)$$

$$\hat{\chi}_c(\boldsymbol{q}, i\nu_m) = \hat{\chi}(\boldsymbol{q}, i\nu_m)[\hat{1} + \hat{U}_c \hat{\chi}(\boldsymbol{q}, i\nu_m)]^{-1}, \quad (11)$$

where $\hat{\chi}(\boldsymbol{q}, i\nu_m)$ is the bare susceptibility matrix given by Eq. (8). We have checked that the Stoner criterion is not matched for the range of interaction strengths studied in the present work.

It is important to notice that $\hat{U}_s$ does *not* depend on $U_\perp$ while $\hat{U}_c$ does [see Eq. (6)]. As such, only the *charge* susceptibility changes as the interlayer interactions increase. This is illustrated in Fig. 2, which shows the main eigenvalue of the spin $[\hat{\chi}_s(\boldsymbol{q}, 0)]$ and charge $[\hat{\chi}_c(\boldsymbol{q}, 0)]$ static susceptibility matrices for different values of $U_\perp/U$ for $U = 1.16$ eV. As such, $\hat{\chi}_s(\boldsymbol{q})$ does not change as $U_\perp/U$ varies, while the main changes in $\hat{\chi}_c(\boldsymbol{q})$ are a reduction near the (π, π) ($\boldsymbol{M}$) point and an overall reduction around the $(0, 0)$ ($\boldsymbol{\Gamma}$) point. These features will be further discussed in Sec. IV B.

B. RPA pairing interaction

We now consider the singlet-channel RPA pairing interaction matrix [23,25] for the multi-orbital, multilayer interacting

model of Eqs. (5) and (6):

$$\Gamma^{p\ell q\ell'}_{s\xi t\xi'}(\boldsymbol{q}) = \tfrac{1}{2}[-\hat{U}_c\hat{\chi}_c(\boldsymbol{q})\hat{U}_c + 3\hat{U}_s\hat{\chi}_s(\boldsymbol{q})\hat{U}_s + \hat{U}_c + \hat{U}_s]^{t\xi' q\ell'}_{p\ell s\xi}. \tag{12}$$

In the mRPA, the pairing interaction $\Gamma(\boldsymbol{k},\boldsymbol{k}')$ between Cooper pairs at $(\boldsymbol{k},-\boldsymbol{k})$ and $(\boldsymbol{k}',-\boldsymbol{k}')$ is computed from Eq. (12) as [23,24]:

$$\Gamma(\boldsymbol{k},\boldsymbol{k}') = \mathrm{Re}\sum_{\ell\ell'\xi\xi'}\sum_{pqst}\left[\psi^{t\xi'}_{\nu_{-\boldsymbol{k}}}(-\boldsymbol{k})\right]^*\left[\psi^{s\xi *}_{\nu_{\boldsymbol{k}}}(\boldsymbol{k})\right]^* \times \Gamma^{p\ell q\ell'}_{s\xi t\xi'}(\boldsymbol{k}-\boldsymbol{k}')\psi^{p\ell}_{\nu_{\boldsymbol{k}'}}(\boldsymbol{k}')\psi^{q\ell'}_{\nu_{-\boldsymbol{k}'}}(-\boldsymbol{k}'). \tag{13}$$

The symmetric part of the pairing interaction $2\bar{\Gamma}(\boldsymbol{k},\boldsymbol{k}') = \Gamma(\boldsymbol{k},\boldsymbol{k}') + \Gamma(\boldsymbol{k},-\boldsymbol{k}')$ is, in turn, used to calculate the gap function $\Delta^\alpha(\boldsymbol{k})$ and the respective pairing strength λ^α using the usual integral eigenvalue equation [23]:

$$-\sum_j \oint_{\boldsymbol{k}'\in C_j}\frac{d\boldsymbol{k}'_{||}}{v_F(\boldsymbol{k}')}\frac{1}{(2\pi)^2}\bar{\Gamma}(\boldsymbol{k},\boldsymbol{k}')\Delta^\alpha(\boldsymbol{k}') = \lambda^\alpha\Delta^\alpha(\boldsymbol{k}), \tag{14}$$

where the sum runs over the different FS sheets C_j and $v_F(\boldsymbol{k})$ denotes the Fermi speed at momentum $\boldsymbol{k}$.

IV. SUPERCONDUCTING PARING SYMMETRIES

A. Leading solutions of the gap equation

For a given set of parameters entering $\bar{\Gamma}(\boldsymbol{k},\boldsymbol{k}')$, the solution of Eq. (14) with the highest eigenvalue $\lambda_{\max}$ will correspond to the highest critical temperature T_c. The symmetry of the pairing gap is reflected in the corresponding eigenfunction $\Delta_{\max}(\boldsymbol{k})$.

In the following, we consider the reference value of $U \approx 1.16$ eV, which has been estimated as $T_c \approx 80$ K from real-space mean-field calculations [12]. Considering the largest interlayer hopping in the model ($|t^z_\perp| \approx 0.635$ eV) [6], gives a moderate $U/|t^z_\perp| \approx 1.83$, reflecting an itinerant electron picture. For these parameters and $U_\perp = 0$, the leading and subleading solutions of Eq. (14) display $s^\pm$-wave and d_{xy}-wave symmetries (with $\lambda^{s^\pm}/\lambda^{d_{xy}} > 1$), in accordance with previous studies [8,11,14].

For increasing values of $U_\perp$, however, the ratio $\lambda^{s^\pm}/\lambda^{d_{xy}}$ *decreases,* and eventually the solution with d_{xy}-wave symmetry becomes dominant. This is illustrated in Fig. 3(a), which shows a color map of $\log(\lambda^{s^\pm}/\lambda^{d_{xy}})$ for different values of onsite U and interlayer $U_\perp$ interaction strengths. The dashed line represents the curve $\lambda^{s^\pm} = \lambda^{d_{xy}}$ and can be interpreted as a "phase boundary" separating the regions where each gap symmetry dominates. The corresponding superconducting gap symmetry solutions projected onto the Fermi surface for the dominant $s^\pm$ and $d_{x^2-y^2}$ waves are shown in Figs. 3(b) and 3(c), respectively.

A more detailed view of the leading and subleading solutions as a function of U and $U_\perp$ is shown in Fig. 4. For $U/U_\perp = 0$ [Fig. 4(a)], $s^\pm$ and $d_{x^2-y^2}$ waves are nearly degenerate for $U < 1$ eV, while the $s^\pm$ dominates for larger values of U. By contrast, increasing the ratio $U_\perp/U > 0$ immediately breaks the degeneracy and suppresses the $s^\pm$ solution, although higher U again favor the sign-changing s-wave, as shown in Figs. 4(b) and 4(c).

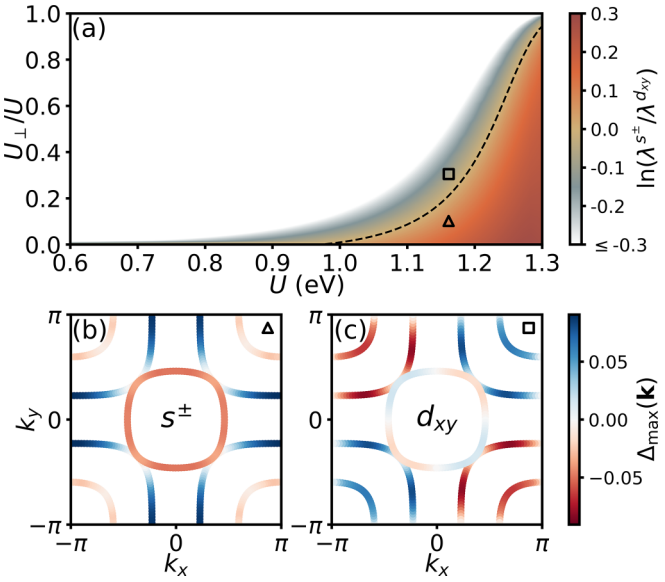

FIG. 3. (a) Phase diagram showing the log of the ratio between the two leading eigenvalues of Eq. (14) for given values of U and $U_\perp$. The corresponding leading gap functions $\Delta_{\max}(\boldsymbol{k})$ displaying $s^\pm$-wave and d_{xy}-wave symmetries for $U = 1.16$ eV, $U_\perp/U = 0.1$ (△), and $U_\perp/U = 0.3$ (□) are shown in panels (b) and (c), respectively.

For the reference value of $U = 1.16$ eV, we show in Fig. 4(d) that the transition point occurs at a moderate value of $U^c_\perp \approx 0.2U = 0.23$ eV, with the gap functions displaying $s^\pm$-wave and d_{xy}-wave symmetries for $U_\perp < U^c_\perp$ and $U_\perp > U^c_\perp$ [Figs. 3(b) and 3(c)], respectively. For larger values of U, however, the $s^\pm$-wave symmetry is clearly favored, even for ratios $U_\perp/U$ as large as 50 to 60%.

Additionally, as discussed in Appendix A, we note that the Hund's couplings J and $J_\perp$ only marginally affect this

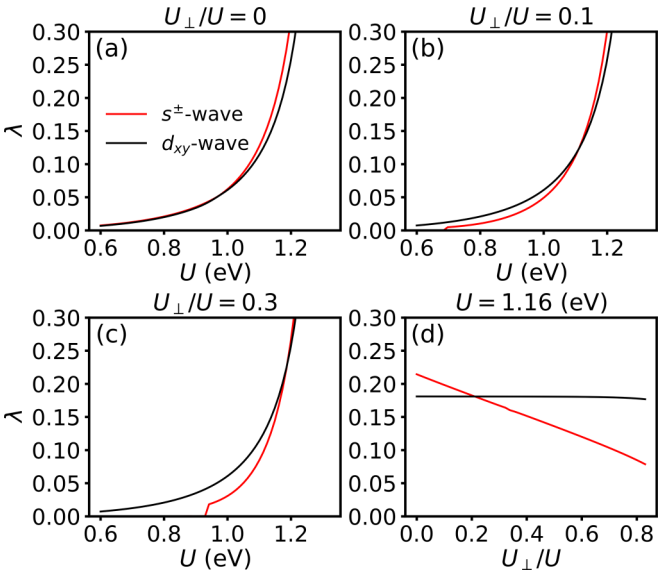

FIG. 4. Line cuts of the phase diagram shown in Fig. 3 showing the leading and subleading eigenvalues of Eq. (14) as a function of (a)–(c) U for different values of $U_\perp/U$ and (d) $U_\perp/U$ for $U = 1.16$ eV.

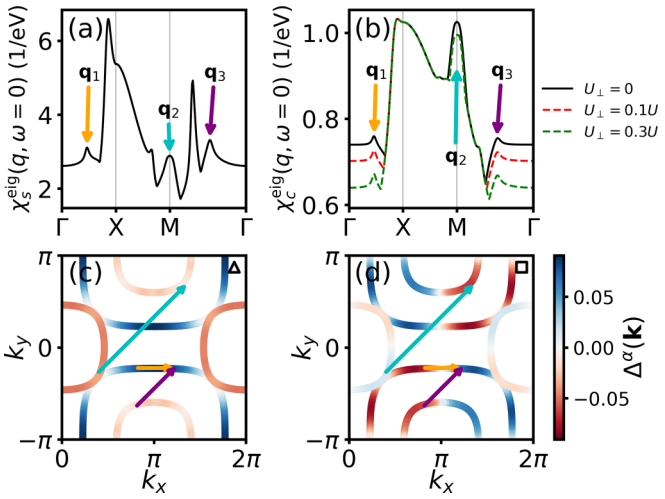

FIG. 5. Susceptibilities and the sign changes in the superconducting gap. The main eigenvalue of the spin and charge susceptibility matrices are shown in panels (a) and (b), respectively. Dashed lines represent results for different $U_\perp/U$ ratios, while the arrows point to the susceptibility peaks related to each putative nesting vector $\boldsymbol{q}_i$. Panels (c) and (d) show the same gap function data of Figs. 1(b) and 1(c), respectively, while the colored arrows corresponded to the vectors $\boldsymbol{q}_i$ in the upper panels.

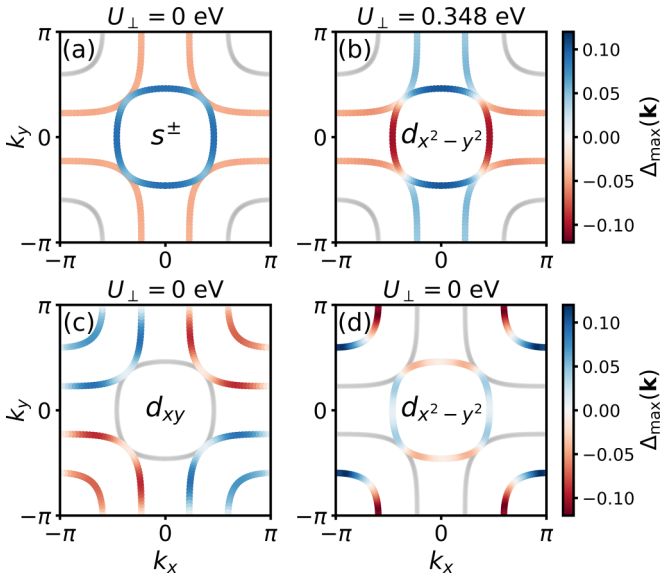

FIG. 6. Color maps of the leading superconducting gap function $\Delta_{max}(\boldsymbol{k})$ computed using the two-orbital bilayer pairing vertex but considering only the contributions of two out of the three FS pockets. Panels (a) and (b) show results excluding the contributions of the γ pocket for $U_\perp = 0$ and $U_\perp = 0.3U = 0.348$ eV, respectively. Panels (c) and (d) show results for $U_\perp = 0$ excluding the contributions of α and β pockets, respectively. In all cases, $U = 1.16$ eV.

general behavior. In fact, increasing J/U does not influence the leading pairing symmetry [Fig. 8]. Moreover, we find that changing $J_\perp/U_\perp$ does not change our conclusions qualitatively, although decreasing $J_\perp/U_\perp$ shifts up the phase boundary separating the two symmetries [dashed black line in Fig. 3(a)].

B. The role of the charge susceptibility

A key aspect in the transition of $s^\pm$ to d_{xy} pairing symmetries as a function of $U_\perp$ is its connection to the decrease in the charge susceptibility peaks near the nesting vectors, previously shown in Fig. 2. As previously mentioned, Eq. (6) shows that the spin susceptibility is unaffected by the interlayer interactions. On the other hand, Figs. 2 (c) and 2(d) show that the charge susceptibility is suppressed for increasing $U_\perp/U$ in regions around the $\boldsymbol{\Gamma}$ and $\boldsymbol{M}$ pockets.

This is better illustrated in Figs. 5(a) and 5(b), which show the main eigenvalue of the spin $[\hat{\chi}_s(\boldsymbol{q},0)]$ and charge $[\hat{\chi}_c(\boldsymbol{q},0)]$ susceptibility matrices, respectively, along the $\boldsymbol{\Gamma}-\boldsymbol{X}-\boldsymbol{M}-\boldsymbol{\Gamma}$ high-symmetry path. The three main nesting vectors ($\boldsymbol{q}_1$, $\boldsymbol{q}_2$, and $\boldsymbol{q}_3$) are marked by small colored arrows.

Figures 5 (c) and 5(d) show the same gap function data as Figs. 1 (b) and 1(c) [$U_\perp/U = 0.1$ (△) and $U_\perp/U = 0.3$ (□), respectively] with a shift in the k_x component so that the three nesting vectors $\boldsymbol{q}_{i=1,2,3}$ (represented as colored arrows, in scale) can be better visualized. A comparison between Figs. 5(c) and 5(d) shows that the $\boldsymbol{q}_1$ and $\boldsymbol{q}_2$ nesting vectors connect pockets where the leading gap function has the *same sign* in the $s^\pm$-wave case (i.e., $\Delta^\alpha(\boldsymbol{k}) = +\Delta^\alpha(\boldsymbol{k}+\boldsymbol{q}_{i=1,2})$) while they are of *opposite sign* in the d_{xy}-wave case ($\Delta^\alpha(\boldsymbol{k}) = -\Delta^\alpha(\boldsymbol{k}+\boldsymbol{q}_{i=1,2})$).

These results can be better understood by looking at both the dependence of the pairing vertex function on the charge susceptibility [Eq. (12)] and on the pairing function $\bar{\Gamma}(\boldsymbol{k},\boldsymbol{k}')$ on the left-hand side of the linear pairing equation [Eq. (14)]. First, we remark that $\hat{\chi}_s(\boldsymbol{q},0)$ contributes with a positive sign to the right-hand side of Eq. (12), while $\hat{\chi}_c(\boldsymbol{q},0)$ contributes with a negative sign. As such, *reductions* in $\hat{\chi}_c(\boldsymbol{q},0)$ tend to *increase* the pairing $\bar{\Gamma}(\boldsymbol{k},\boldsymbol{k}+\boldsymbol{q})$, particularly at the nesting points $\boldsymbol{q} = \boldsymbol{q}_{1,2}$, at which the spin susceptibility is lower than at $\boldsymbol{q} = \boldsymbol{q}_3$ [see Fig. 5(a)].

Due to the negative sign on the left-hand side in Eq. (14) and considering that $\bar{\Gamma}(\boldsymbol{k},\boldsymbol{k}+\boldsymbol{q})$ is positive at the nesting points, we argue that such increases in $\bar{\Gamma}(\boldsymbol{k},\boldsymbol{k}+\boldsymbol{q}_{1,2})$ as $U_\perp/U$ increases will favor sign-changing solutions which obey $\Delta^\alpha(\boldsymbol{k}) = -\Delta^\alpha(\boldsymbol{k}+\boldsymbol{q}_{1,2})$ such as the d_{xy}-wave symmetric one.

C. Orbital contributions to the pairing interaction

Further insight as to why the interlayer interaction tends to favor a d-wave symmetry over the $s^\pm$ one can be gained by looking more closely at the role of the interorbital contribution to the pairing interaction. Imagine if one could tune the relative contributions of the different FS sheets to the paring gap function defined by Eq. (14). In practice, this can be accomplished by artificially giving different weights to the terms in the sum on the left-hand side of Eq. (14). For instance, one could exclude (assign zero weight to) the contribution of one of the FS pockets (α, β, or γ) and see what the resulting symmetry of the leading pairing gap function looks like.

This is done in Fig. 6 for $U = 1.16$ eV. Figure 6(a) shows that, for $U_\perp = 0$, the pairing gap symmetry remains $s^\pm$-wave even if the contribution of the γ pocket is excluded and only pockets α and β, which are dominated by $3d_{x^2-y^2}$ orbitals and hence have a more "planar" character, are considered in the calculation. In a sense, this would mimic a "cuprate-like"

TABLE I. Summary of superconducting pairing symmetries found for each pocket or combination of pockets α, β, γ as indicated in Fig. 1(b). We set $U = 1.16$ eV.

Pockets	$U_\perp/U$	Symmetry
α	any	g-wave
β	any	d_{xy}-wave
γ	any	$d_{x^2-y^2}$-wave
$\alpha+\beta$	$\lesssim 0.3$	$s^\pm$-wave
$\alpha+\beta$	$\gtrsim 0.3$	d_{xy}-wave
$\alpha+\gamma$	any	$d_{x^2-y^2}$-wave
$\beta+\gamma$	any	d_{xy}-wave
all	$\lesssim 0.2$	$s^\pm$-wave
all	$\gtrsim 0.2$	d_{xy}-wave

scenario [17]. In this situation, by increasing $U_\perp$ the symmetry of the leading gap function becomes $d_{x^2-y^2}$ and *not* d_{xy}, as in the case where all pockets are considered [Fig. 3(c)]. On the other hand, the pairing symmetry becomes d_{xy} if, instead, the contribution of the α pocket is excluded [Fig. 6(c)]. Finally, if the contribution of the β pocket is excluded, the gap symmetry becomes $d_{x^2-y^2}$ [Fig. 6(d)] and not d_{xy}. A summary of these findings is presented in Table I, which also includes other combinations of the α, β, γ pockets (as detailed in Appendix B).

These results indicate that, when all three pockets are considered in the calculation (Fig. 3), by increasing $U_\perp$, the relative contribution of the γ pocket (dominated by $d_{3z^2-r^2}$ orbitals) increases over the (more planar) α pocket contribution, thereby inducing the switching between $s^\pm$- and nodal d_{xy}-wave pairing symmetries. As such, the interplay between γ and α pockets in the pairing vertex is a crucial element in explaining the $s^\pm \to d_{xy}$ order switching as $U_\perp$ increases.

This conclusion is further supported by looking at the differences in the pairing vertex function $\Gamma(\boldsymbol{k}, \boldsymbol{k}')$ for $U_\perp = 0.348$ eV and $U_\perp = 0$. Figure 7 shows the ratio between $\Gamma(\boldsymbol{k}, \boldsymbol{k}')$ (calculated with $U_\perp = 0.348$ eV) and $\Gamma^{\text{on}}(\boldsymbol{k}, \boldsymbol{k}')$ (calculated with $U_\perp = 0$), for a fixed $\boldsymbol{k}$ (marked as a black circle) and as a function of $\boldsymbol{k}'$ along the FS.

For example, as shown in Fig. 7(a), for a $\boldsymbol{k}$-point located in the γ pocket, increasing $U_\perp$ leads to an *enhancement* of the pairing vertex function $[\Gamma(\boldsymbol{k}, \boldsymbol{k}') > \Gamma^{\text{on}}(\boldsymbol{k}, \boldsymbol{k}')]$ along the α pocket and a *decrease* $[\Gamma(\boldsymbol{k}, \boldsymbol{k}') < \Gamma^{\text{on}}(\boldsymbol{k}, \boldsymbol{k}')]$ along the β pocket. A similar result occurs when $\boldsymbol{k}$ is located at the α pocket [Fig. 7(b)]: The pairing vertex function is enhanced along the γ pocket and decreases along the β pocket.

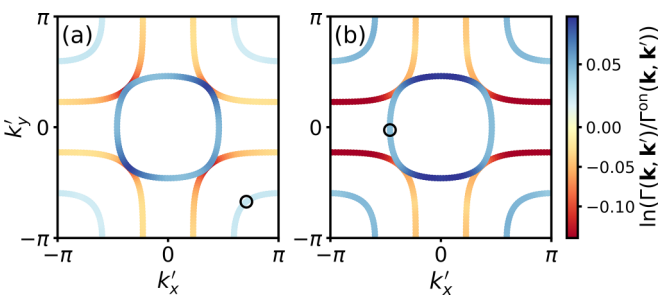

FIG. 7. Enhancement of the pairing vertex function ($\Gamma(\boldsymbol{k}, \boldsymbol{k}')$) by interlayer interactions. Panels (a) and (b) show the ratio of $\Gamma(\boldsymbol{k}, \boldsymbol{k}')$ calculated with $U_\perp = 0.348$ eV and $\Gamma^{\text{on}}(\boldsymbol{k}, \boldsymbol{k}')$, calculated with $U_\perp = 0$ in a logarithmic scale for a fixed $\boldsymbol{k}$ (black ring) located at (a) γ and (b) α FS pockets, dominated by $d_{3z^2-r^2}$ and $d_{x^2-y^2}$ orbitals, respectively.

This result is consistent with our picture that interlayer interactions tend to favor the d_{xy} pairing symmetry over the $s^\pm$ by favoring the interorbital pairing between electrons in the γ and α pockets, which are dominated by the $d_{3z^2-r^2}$ and $d_{x^2-y^2}$ orbital contributions, respectively.

V. CONCLUDING REMARKS

In this work, we investigate the role of interlayer Coulomb interaction terms on the superconducting properties of $La_3Ni_2O_7$ under pressure in the weak-to-intermediate-coupling limit. Our results indicate that for moderate onsite interactions in the model (up to $U \sim 1.1$ eV), and relatively small interlayer interaction strengths (about $\sim$30% of the onsite term), the leading pairing symmetry becomes of the d_{xy}-wave type instead of the $s^\pm$-wave predicted by several works in the *absence* of interlayer interactions [8,12,14,15]. Our calculations also confirm that the $s^\pm$ solution is dominant for large onsite interactions ($U \gtrsim 1.3$ eV). This is consistent with results from strong-coupling ($t - \tilde{J} - \tilde{J}_\perp$) bi-layer single-orbital models which show $s^\pm$-wave superconductivity favored by a strong interlayer exchange coupling [14,15].

Additionally, our results indicate that charge fluctuations play an essential role in the s- to $-d$-wave transition as the interlayer interaction $U_\perp$ increases. This is a consequence of a decrease in the charge susceptibility for large $U_\perp$ values, particularly at momenta $\boldsymbol{q}_i$ satisfying the nesting condition between different FS sheets. This in turn leads to an *increase* of the RPA pairing function at these nesting vectors, favoring d_{xy}-wave sign-changing solutions obeying $\Delta^\alpha(\boldsymbol{k}) = -\Delta^\alpha(\boldsymbol{k} + \boldsymbol{q}_i)$ over the $s^\pm$-wave ones. We note that these $s^\pm$-wave solutions differ from those appearing in iron-based superconductors [23,24], for which sign changes can be traced back to the *spin* susceptibility at the nesting points.

More interestingly, our analysis shows that the superconducting pairing symmetry is strongly dependent on the interplay of *all three* FS pockets. In particular, the interlayer interaction tends to favor interorbital pairing between electrons with $d_{3z^2-r^2}$ and $d_{x^2-y^2}$ orbital character, underscoring the view that a complete description of the superconducting properties can only be achieved by multi-orbital models [8–10,17]. In fact, we expect that a similar picture can emerge in systems exhibiting multiple FS pockets with close competing pairing symmetries, such as the three-layer $La_4Ni_3O_{10}$ [34].

ACKNOWLEDGMENTS

We thank I. Eremin and S. Bötzel for fruitful discussions. We acknowledge financial support from the São Paulo Research Foundation (FAPESP), Brazil (Grants No. 2022/15453-0 and No. 2023/14902-8) and from CNPq (Grant No. 312622/2023-6).

DATA AVAILABILITY

The data that support the findings of this article are openly available [37].

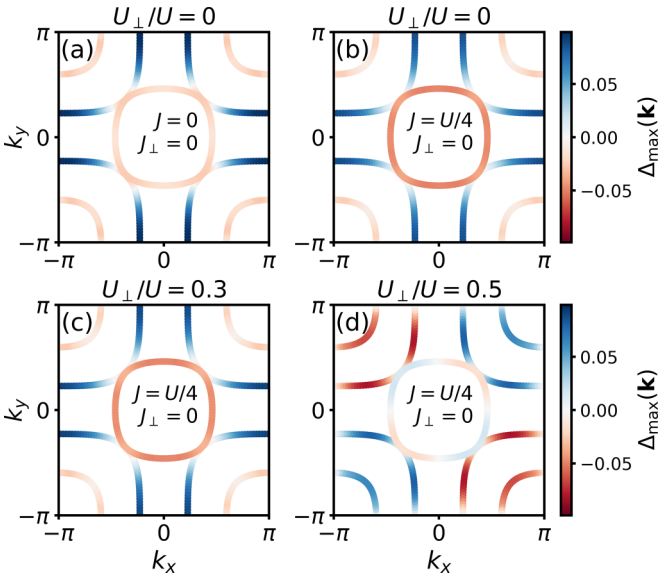

FIG. 8. Leading gap functions $\Delta_{max}(\boldsymbol{k})$ displaying $s^{\pm}$-wave and d_{xy}-wave symmetries for $U = 1.16$ eV, $U_\perp/U = 0.1$ (△), and $U_\perp/U = 0.3$ (□).

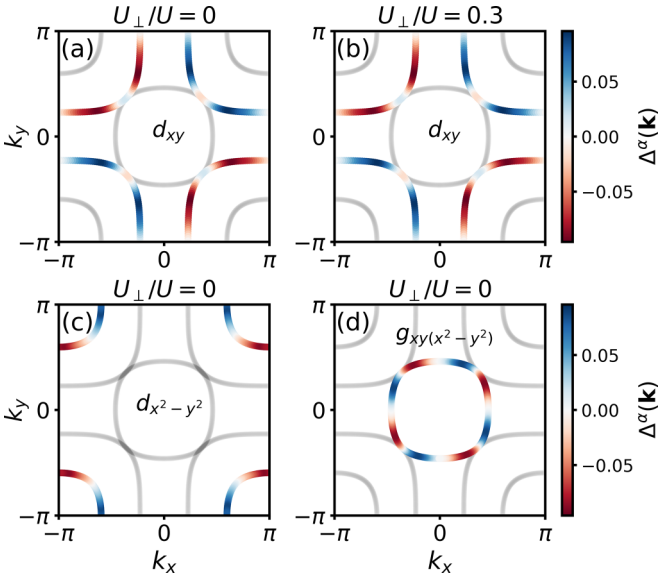

FIG. 9. Same as Fig. 6 but for individual pockets β (a), (b), γ (c), and α (d).

APPENDIX A: INFLUENCE OF HUND'S COUPLINGS IN THE PAIRING SYMMETRY

The influence of Hund's couplings J and $J_\perp$ in the pairing symmetry is shown in Fig. 8. For $U/U_\perp = 0$, Fig. 8(a) shows that $J = J_\perp = 0$ results in a leading $s^{\pm}$-wave, while increasing J/U does not influence the pairing symmetry but for enhancing the gap function at the α pocket in comparison with the other pockets, which is illustrated in panel (b). On the other hand, fixing $J = U/4$ and $J_\perp = 0$, the $U_\perp/U = 0.3$ gap symmetry shown in Fig. 8(c) results in a leading $s^{\pm}$-wave, while only further increases interlayer interactions, $U_\perp/U = 0.5$ as in Fig. 8(d), induce the subleading d_{xy} as the leading pairing symmetry. Therefore, lowering $J_\perp/U_\perp$ only increases the ratio $U_\perp/U$ necessary for the $s^{\pm} \to d_{xy}$ transition, which does not qualitatively change the phase diagram of Fig. 3(a).

APPENDIX B: PAIRING SYMMETRY OF INDIVIDUAL POCKETS

Figure 6 shows results for couples of pockets, but we have also checked that conclusions hold for the individual pockets as well. In Fig. 9, panels (a) and (b) show no change in the d_{xy} symmetry of the β pocket as the interlayer coupling varies from $U_\perp/U = 0$ (a) to $U_\perp/U = 0.3$ (b). In fact, the interlayer interactions do not change the symmetry in any three cases explored. As shown in panel (c), a $d_{x^2-y^2}$-wave dominates the pairing of individual γ pockets, and a g-wave symmetry is obtained for the α pocket alone (d). None of the single-pocket solutions reproduces the $s^{\pm} \to d_{xy}$ transition as a function of interlayer interactions.

[1] H. Sun, M. Huo, X. Hu, J. Li, Z. Liu, Y. Han, L. Tang, Z. Mao, P. Yang, B. Wang, J. Cheng, D.-X. Yao, G.-M. Zhang, and M. Wang, Signatures of superconductivity near 80 K in a nickelate under high pressure, Nature (London) **621**, 493 (2023).

[2] G. Wang, N. N. Wang, X. L. Shen, J. Hou, L. Ma, L. F. Shi, Z. A. Ren, Y. D. Gu, H. M. Ma, P. T. Yang, Z. Y. Liu, H. Z. Guo, J. P. Sun, G. M. Zhang, S. Calder, J.-Q. Yan, B. S. Wang, Y. Uwatoko, and J.-G. Cheng, Pressure-induced superconductivity in polycrystalline $La_3Ni_2O_{7-\delta}$, Phys. Rev. X **14**, 011040 (2024).

[3] J. Li, P. Ma, H. Zhang, X. Huang, C. Huang, M. Huo, D. Hu, Z. Dong, C. He, J. Liao, X. Chen, T. Xie, H. Sun, and M. Wang, Identification of superconductivity in bilayer nickelate $La_3Ni_2O_7$ under high pressure up to 100 GPa, Natl. Sci. Rev. nwaf220 (2025).

[4] M. Wang, H.-H. Wen, T. Wu, D.-X. Yao, and T. Xiang, Normal and superconducting properties of $La_3Ni_2O_7$, Chin. Phys. Lett. **41**, 077402 (2024).

[5] E. K. Ko, Y. Yu, Y. Liu, L. Bhatt, J. Li, V. Thampy, C.-T. Kuo, B. Y. Wang, Y. Lee, K. Lee, J.-S. Lee, B. H. Goodge, D. A. Muller, and H. Y. Hwang, Signatures of ambient pressure superconductivity in thin film $La_3Ni_2O_7$, Nature (London) **638**, 935 (2025).

[6] Z. Luo, X. Hu, M. Wang, W. Wú, and D.-X. Yao, Bilayer two-orbital model of $La_3Ni_2O_7$ under pressure, Phys. Rev. Lett. **131**, 126001 (2023).

[7] Y. Zhang, L.-F. Lin, A. Moreo, and E. Dagotto, Electronic structure, dimer physics, orbital-selective behavior, and magnetic tendencies in the bilayer nickelate superconductor $La_3Ni_2O_7$ under pressure, Phys. Rev. B **108**, L180510 (2023).

[8] Y. Zhang, L.-F. Lin, A. Moreo, T. A. Maier, and E. Dagotto, Structural phase transition, $S_{\pm}$-wave pairing, and magnetic stripe order in bilayered superconductor $La_3Ni_2O_7$ under pressure, Nat. Commun. **15**, 2470 (2024).

[9] F. Lechermann, J. Gondolf, S. Bötzel, and I. M. Eremin, Electronic correlations and superconducting instability in $La_3Ni_2O_7$ under high pressure, Phys. Rev. B **108**, L201121 (2023).

[10] Z. Luo, B. Lv, M. Wang, W. Wú, and D.-X. Yao, High-T_c superconductivity in $La_3Ni_2O_7$ based on the bilayer two-orbital t-J model, npj Quantum Mater. **9**, 61 (2024).

[11] Q.-G. Yang, D. Wang, and Q.-H. Wang, Possible $s_\pm$-wave superconductivity in $La_3Ni_2O_7$, Phys. Rev. B **108**, L140505 (2023).

[12] Y.-B. Liu, J.-W. Mei, F. Ye, W.-Q. Chen, and F. Yang, $s^\pm$-wave pairing and the destructive role of apical-oxygen deficiencies in $La_3Ni_2O_7$ under pressure, Phys. Rev. Lett. **131**, 236002 (2023).

[13] F. Lechermann, S. Bötzel, and I. M. Eremin, Electronic instability, layer selectivity, and Fermi arcs in $La_3Ni_2O_7$, Phys. Rev. Mater. **8**, 074802 (2024).

[14] X.-Z. Qu, D.-W. Qu, J. Chen, C. Wu, F. Yang, W. Li, and G. Su, Bilayer t–J–$J_\perp$ model and magnetically mediated pairing in the pressurized nickelate $La_3Ni_2O_7$, Phys. Rev. Lett. **132**, 036502 (2024).

[15] J. Chen, F. Yang, and W. Li, Orbital-selective superconductivity in the pressurized bilayer nickelate $La_3Ni_2O_7$: An infinite projected entangled-pair state study, Phys. Rev. B **110**, L041111 (2024).

[16] H. Sakakibara, N. Kitamine, M. Ochi, and K. Kuroki, Possible high T_c superconductivity in $La_3Ni_2O_7$ under high pressure through manifestation of a nearly half-filled bilayer Hubbard model, Phys. Rev. Lett. **132**, 106002 (2024).

[17] Z. Fan, J.-F. Zhang, B. Zhan, D. Lv, X.-Y. Jiang, B. Normand, and T. Xiang, Superconductivity in nickelate and cuprate superconductors with strong bilayer coupling, Phys. Rev. B **110**, 024514 (2024).

[18] S. Bötzel, F. Lechermann, J. Gondolf, and I. M. Eremin, Theory of magnetic excitations in the multilayer nickelate superconductor $La_3Ni_2O_7$, Phys. Rev. B **109**, L180502 (2024).

[19] C. Xia, H. Liu, S. Zhou, and H. Chen, Sensitive dependence of pairing symmetry on Ni-e_g crystal field splitting in the nickelate superconductor $La_3Ni_2O_7$, Nat. Commun. **16**, 1054 (2025).

[20] T. Xie, M. Huo, X. Ni, F. Shen, X. Huang, H. Sun, H. C. Walker, D. Adroja, D. Yu, B. Shen, L. He, K. Cao, and M. Wang, Strong interlayer magnetic exchange coupling in $La_3Ni_2O_7$-δ revealed by inelastic neutron scattering, Sci. Bull. **69**, 3221 (2024).

[21] X. Chen, J. Choi, Z. Jiang, J. Mei, K. Jiang, J. Li, S. Agrestini, M. Garcia-Fernandez, H. Sun, X. Huang, D. Shen, M. Wang, J. Hu, Y. Lu, K.-J. Zhou, and D. Feng, Electronic and magnetic excitations in $La_3Ni_2O_7$, Nat. Commun. **15**, 9597 (2024).

[22] H. Zhong, B. Hao, Y. Wei, Z. Zhang, R. Liu, X. Huang, X.-S. Ni, M. dos Reis Cantarino, K. Cao, Y. Nie, T. Schmitt, and X. Lu, Epitaxial strain tuning of electronic and spin excitations in $La_3Ni_2O_7$ thin films, arXiv:2502.03178.

[23] S. Graser, T. A. Maier, P. J. Hirschfeld, and D. J. Scalapino, Near-degeneracy of several pairing channels in multiorbital models for the Fe pnictides, New J. Phys. **11**, 025016 (2009).

[24] A. F. Kemper, T. A. Maier, S. Graser, H.-P. Cheng, P. J. Hirschfeld, and D. J. Scalapino, Sensitivity of the superconducting state and magnetic susceptibility to key aspects of electronic structure in ferropnictides, New J. Phys. **12**, 073030 (2010).

[25] M. Altmeyer, D. Guterding, P. J. Hirschfeld, T. A. Maier, R. Valentí, and D. J. Scalapino, Role of vertex corrections in the matrix formulation of the random phase approximation for the multiorbital Hubbard model, Phys. Rev. B **94**, 214515 (2016).

[26] G. B. Martins, A. Moreo, and E. Dagotto, RPA analysis of a two-orbital model for the BiS_2-based superconductors, Phys. Rev. B **87**, 081102(R) (2013).

[27] L. B. Braz, G. B. Martins, and L. G. G. V. D. da Silva, Charge and spin fluctuations in superconductors with intersublattice and interorbital interactions, arXiv:2403.02453v1.

[28] W. Xi, S.-L. Yu, and J.-X. Li, Transition from s_{pm}-wave to $d_x^2 - y^2$-wave superconductivity driven by interlayer interaction in the bilayer two-orbital model of $La_3Ni_2O_7$, Phys. Rev. B **111**, 104505 (2025).

[29] J. Zhan, C. Le, X. Wu, and J. Hu, Impact of nonlocal Coulomb repulsion on superconductivity and density-wave orders in bilayer nickelates, arXiv:2503.18877.

[30] S. Cai, Y. Zhou, H. Sun, K. Zhang, J. Zhao, M. Huo, L. Nataf, Y. Wang, J. Li, J. Guo, K. Jiang, M. Wang, Y. Ding, W. Yang, Y. Lu, Q. Kong, Q. Wu, J. Hu, T. Xiang, H. K. Mao *et al.*, Low-temperature mean valence of nickel ions in pressurized $La_3Ni_2O_7$, Phys. Rev. B **111**, 104511 (2025).

[31] J. Yang, H. Sun, X. Hu, Y. Xie, T. Miao, H. Luo, H. Chen, B. Liang, W. Zhu, G. Qu, C.-Q. Chen, M. Huo, Y. Huang, S. Zhang, F. Zhang, F. Yang, Z. Wang, Q. Peng, H. Mao, G. Liu *et al.*, Orbital-dependent electron correlation in double-layer nickelate $La_3Ni_2O_7$, Nat. Commun. **15**, 4373 (2024).

[32] Y. Li, X. Du, Y. Cao, C. Pei, M. Zhang, W. Zhao, K. Zhai, R. Xu, Z. Liu, Z. Li, J. Zhao, G. Li, Y. Qi, H. Guo, Y. Chen, and L. Yang, Electronic correlation and pseudogap-like behavior of high-temperature superconductor $La_3Ni_2O_7$, Chin. Phys. Lett. **41**, 087402 (2024).

[33] Y. Zhang, L.-F. Lin, A. Moreo, T. A. Maier, and E. Dagotto, Electronic structure, magnetic correlations, and superconducting pairing in the reduced Ruddlesden-Popper bilayer $La_3Ni_2O_6$ under pressure: Different role of $d_{3z^2-r^2}$ orbital compared with $La_3Ni_2O_7$, Phys. Rev. B **109**, 045151 (2024).

[34] Y. Zhang, L.-F. Lin, A. Moreo, T. A. Maier, and E. Dagotto, Prediction of $s^\pm$-wave superconductivity enhanced by electronic doping in trilayer nickelates $La_4Ni_3O_{10}$ under pressure, Phys. Rev. Lett. **133**, 136001 (2024).

[35] The remaining matrix elements can be trivially obtained by exchanging $A \leftrightarrow B$.

[36] T. Ozaki, Continued fraction representation of the Fermi-Dirac function for large-scale electronic structure calculations, Phys. Rev. B **75**, 035123 (2007).

[37] L. Barreto Braz, L. Dias da Silva, and G. Balster Martins, Interlayer interactions in $La_3Ni_2O_7$ under pressure: From $s^\pm$ to d_xy-wave superconductivity [Data set], Zenodo (2025), https://doi.org/10.5281/zenodo.14933119.